Computers and Geotechnics 126 (2020) 103724

Contents lists available at ScienceDirect

Computers and Geotechnics

journal homepage: www.elsevier.com/locate/compgeo

Research Paper

Back analysis of displacements for estimating spatial distribution of viscoelastic properties around an unlined rock cavern

Xu Gao[a], E-Chuan Yan[a], Tian-Chyi Jim Yeh[b,c,*], Xiao-Meng Yin[d], Jing-Sen Cai[a], Yong-Hong Hao[b], Jet-Chau Wen[e,f]

[a] Faculty of Engineering, China University of Geosciences, Wuhan 430074, China
[b] Key Laboratory for Water Environment and Resources, Tianjin Normal University, Tianjin, China
[c] Department of Hydrology and Atmospheric Sciences, University of Arizona, Tucson, AZ 85721, USA
[d] Xinyang Normal University, College of Architecture and Civil Engineering, Xinyang 464000, China
[e] Department of Safety, Health, and Environmental Engineering, National Yunlin University of Science and Technology, Douliu, Taiwan
[f] Research Center for Soil and Water Resources and Natural Disaster Prevention, National Yunlin University of Science and Technology, Douliu, Taiwan

ARTICLE INFO

Keywords:
Unlined rock cavern
Viscoelastic parameters
Displacement back analysis
Heterogeneity
Successive linear estimator

ABSTRACT

A displacement back analysis algorithm is developed, considering the time-dependent effect of the rock mass. It can map spatially distributed the first elastic modulus (E_1), viscidity coefficient (η_1), and the second elastic modulus (E_2) of the Kelvin-Voigt viscoelastic constitutive model (VCM) and the Poynting-Thomson VCM in a rock mass by fusion of the observed displacement data from the excavation of an unlined rock cavern. The algorithm is tested and validated using numerical experiments with a synthetic heterogeneous rock mass. The results of the experiments show that this approach yields unbiased estimates of E_1, η_1, and E_2 fields and quantifies their uncertainty. Further, the estimated fields closely predict shear strain distribution and displacements field in the example.

1. Introduction

The time-dependent behavior of the rock mass is particularly important in unlined rock caverns (URCs) excavated in soft rock, heavily sheared weak rock masses, or rock masses with high in-situ stress (Guan et al., 2008). After URC excavation in such rock masses, the ground could gradually deform, leading to the closure of URCs, reduction of the URCs cross-section (Pellet et al., 2009), or reinforcement of the cavern during its service life (Guan et al., 2008). As a result, the time-dependent behaviors of rock mass must be considered in the design and maintenance of URCs in the weak and soft rock mass.

In order to understand and forecast the time-dependent deformation in URCs, the knowledge of the viscoelastic behavior of the geologic medium (i.e., constitutive model and its parameters, such as viscidity coefficient and elastic modulus) is necessary. However, laboratory tests or large-scale field mechanical tests for investigating the behavior are seldom conducted (Jiang et al., 2013; Yang et al., 2008; Zhang et al., 2008) due to cost and time. In addition, these properties vary spatially, and their spatial distributions (heterogeneity) are difficult to characterize fully. For these reasons, approaches such as inverse modeling or back analysis have been developed. They take advantage of measured displacements and/or stresses of the geological formations during the construction stage of URCs to estimate the parameters.

Over the past decades, various displacement back analysis methods have been developed. They were built on the homogeneous or zonation parameter field assumption without considering detailed spatial variability of the parameters and the uncertainty associated with the estimate. For example, Yang et al. (2001) presented finite element equations for back-analysis based on four rheological models. Ghorbani and Sharifzadeh (2009) applied the univariate optimization algorithm to identify the properties of the Burger-creep visco-plastic (CVISC) model and the initial stress ratio. Similarly, FENG et al. (2006) proposed a hybrid genetic identification method with an improved particle swarm optimization (PSO) algorithm to simultaneously identify the viscoelastic rock material model structure and their parameters. Using measurements of relative displacements of pillar walls, Nazarova and Nazarov (2005) developed a method to estimate rheological properties of rocks and then analyzed the stability of the pillar. Recently, a discrete element method was developed by Nadimi et al. (2011) for back analysis of the time-dependent behavior of the Siah Bisheh cavern due to

* Corresponding author at: Department of Hydrology and Atmospheric Sciences, The University of Arizona, 1133 E. James E. Rogers Way, 122 Harshbarger Bldg 11, Tucson, Arizona 85721, USA.
E-mail address: yeh@hwr.arizona.edu (T.-C.J. Yeh).

https://doi.org/10.1016/j.compgeo.2020.103724
Received 20 February 2020; Received in revised form 19 May 2020; Accepted 26 June 2020

the presence of fractures and joints.

More recently, geostatistical methods (i.e., kriging or co-kriging), which use measured parameters and their spatial structures (variograms or covariances), have been applied by Liu et al., 2016; Chen et al., 2016; Pinheiro et al., 2016; Eivazy et al., 2017; Mayer and Stead, 2017) to estimate spatially distributed mechanical parameter fields using available point samples of parameters. Generally, the geostatistical methods require a large number of spatial samples to derive reliable spatial distribution of the parameter fields. This large number of samples may not be possible in the preliminary design stage of underground projects. Moreover, in-situ rock properties may change due to blasting and stress relaxation during the excavation process. Because of these reasons, combining the displacements data during excavation and the geostatistical theory as the back analysis is highly desirable. Recently, Gao et al. (2018a), Gao et al. (2018b) developed a geostatistical back analysis to map spatially distributed deformability and/or shear strength in a rock mass by fusion of the observed displacement data from the excavation of a URC. However, these studies assumed the linear-elastic or the elastic-perfectly plastic law in their approaches, which is inappropriate for describing the time-dependent behavior of the rock mass. Therefore, a need for a geostatistical back analysis, which considers the time-dependent properties of the rock mass, is clear.

In this paper, we develop a geostatistic estimation approach (Successive Linear Estimator, SLE) to exploit the data of displacement induced by excavations for the back analysis, considering the time-dependent behavior of rock mass. The SLE has been widely used in mapping hydraulic properties in the subsurface, known as hydraulic tomography, HT, (Yeh and Liu, 2000; Zhu and Yeh, 2005) but has not been used in the displacement back analysis of viscoelastic properties of the rock mass.

In the following sections, we discuss the viscoelastic mechanical model first, and then, a synthetic, two-dimensional numerical model for a URC with spatially varying viscoelastic parameters are created as our reference fields. The importance of the effect of heterogeneity of rock mass on deformability and stability of the URC is then demonstrated. Subsequently, we introduce our stochastic back analysis approach. We afterward present the results of parameter estimation and their associated uncertainty. Finally, the estimated parameter fields and associated uncertainty are combined to predict displacements and their uncertainty, using the first-order approximation method.

2. Mechanical model

2.1. Viscoelastic numerical model

In this study, the Kelvin-Voigt (KV) constitutive model and the Poynting-Thomson (PT) constitutive model are selected to describe the time-dependent deformation of the rock mass, respectively. The concepts of these models are illustrated in Fig. 1a and 1b, in which σ_c is applied stress, η_1 is the viscidity coefficient, and E_1 and E_2 are elastic moduli in these models.

Based on these two models, a two-dimensional finite element model is built for simulating the spatiotemporal evolution of stress and strain in a heterogeneous rock mass after the excavation of an unlined rock cavern. This finite element model considers both instantaneous elastic deformation and viscous deformation; the total strain of each element, $\{\varepsilon\}$, thus contains two parts:

$$\{\varepsilon\} = \{\varepsilon_e\} + \{\varepsilon_v\} \tag{1}$$

where $\{\varepsilon_e\}$ is the instantaneous elastic strain vector; $\{\varepsilon_v\}$ is the viscous strain vector. The stress vector of each element, $\{\sigma\}$, can be represented as:

$$\{\sigma\} = [D](\{\varepsilon\} - \{\varepsilon_v\}) \tag{2}$$

where $[\boldsymbol{D}]$ contains the instantaneous elastic modulus (E_e) and Poisson's ratio (υ). For the KV model, $E_e = E_2$; for the PT model, $E_e = E_1 + E_2$ (Yang et al., 2001). If the external force (e.g., excavation force) is $\{f_{ex}\}$, the stress equilibrium equation becomes:

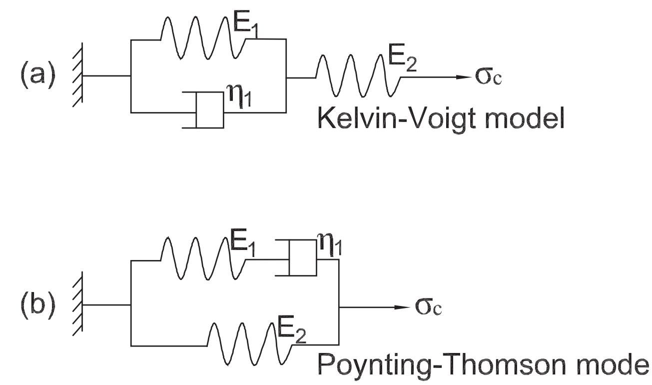

Fig. 1. Two viscoelastic constitutive models: (a) Kelvin-Voigt model; (b) Poynting-Thomson model.

$$\{f_{ex}\} = \iint [B]^T\{\sigma\}dxdz \tag{3}$$

where $[B]$ is the geometry matrix relating strains and nodal displacements; the superscript T denotes the transpose symbol; x represents the horizontal direction and is positive from the left to the right direction, and z represents the vertical direction and is positive upward.

Substituting Eq. (2) into Eq. (3), the stress equilibrium equation can be represented in a matrix form:

$$[K_m]\cdot\{u\} = \{f_{ex}\} + \{f_v\} \tag{4}$$

where $[K_m]$ is the element stiffness matrix, i.e., $[K_m] = \iint [B]^T[D][B]dxdz$; $\{u\}$ is the nodal displacement components; $\{f_v\}$ is the node force induced by the viscous strain. That is,

$$\{f_v\} = \iint [B]^T[D]\{\varepsilon_v\}dxdz \tag{5}$$

To solve Eq. (4), the forces on the right-hand side of the equation have to be specified. They are determined as follows. Suppose we denote the elements to be excavated as Ω, and the initial geostress of these elements before excavation is $\{\sigma_\Omega\} = [\sigma_{hor}, \sigma_{ver}, 0]^T$ (among them, σ_{hor} is the initial horizontal geostress; σ_{ver} is the initial vertical geostress). Then, the forces acting on the cavern boundary after excavation become the sum of $\{\sigma_\Omega\}$ and the weight of the elements (Smith et al., 2013). That is,

$$\{f_{ex}\} = \int_{V_\Omega} [B]^T\{\sigma_\Omega\}dV_\Omega + \gamma_g\int_{V_\Omega} [N]^T dV_\Omega \tag{6}$$

where γ_g is the rock unit weight; V_Ω is the excavated volume; $[\mathbf{N}]$ is the element shape functions, corresponding to the typical 4-node quadrilateral element in this study. The initial horizontal stresses (σ_{hor}) are calculated by multiplying the vertical stress (σ_{ver}) with a constant coefficient of lateral earth pressure (k_0), i.e., $\sigma_{hor} = k_0\sigma_{ver}$, while the initial vertical stress (σ_v) is the weight of the element.

Additionally, in order to calculate the force induced by the viscous strain $\{f_v\}$, the viscous strain has to be determined. Since time-dependent effects are considered, the time-dependent viscous strain is defined based on the KV model as

$$\{\varepsilon_v\}^{t+\triangle t} = e^{-\frac{E_1\triangle t}{\eta_1}}\{\varepsilon_v\}^t + \frac{[A]\{\sigma\}^t}{E_1}\left(1 - e^{-\frac{E_1\triangle t}{\eta_1}}\right) \tag{7}$$

In which the current viscous strain is $\{\varepsilon_v\}^{t+\triangle t}$, the previous viscous strain is $\{\varepsilon_v\}^t$, and the previous stress state of element is $\{\sigma\}^t$.

On the other hand, the viscous strain of the PT model is described by the relationship:

$$\{\varepsilon_v\}^{t+\triangle t} = e^{-\frac{E_1E_2\triangle t}{(E_1+E_2)\eta_1}}\{\varepsilon_v\}^t + \frac{E_1[A]\{\sigma\}^t}{E_2(E_1+E_2)}\left(1 - e^{-\frac{E_1E_2\triangle t}{(E_1+E_2)\eta_1}}\right) \quad (8)$$

In Eqs. (7) and (8), $\triangle t$ is the time interval; $[A]$ is a constant matrix and contains the Poisson's ratio only. If the plane strain assumption is adopted, the $[A]$ matrix is given as:

$$[A] = \begin{bmatrix} 1 & -\upsilon/(1-\upsilon) & 0 \\ -\upsilon/(1-\upsilon) & 1 & 0 \\ 0 & 0 & 2/(1-\upsilon) \end{bmatrix} \quad (9)$$

Notice that at the initial time (i.e., t = 0), the forces $\{f_v\}^{t=0}$ are equal to zero, and afterward, they change according to Eq. (5), and Eq. (7) or Eq. (8). As the simulation progresses, the viscous strain in Eqs. (7) or (8) reach a steady-state condition, if

$$Ratio = \left[\frac{\left(\sum_{Elements}\sum_{Gauss}\sqrt{\frac{2}{3}(\varepsilon_x^2+\varepsilon_z^2+\varepsilon_{xz}^2)}\right)^{n+1}}{\left(\sum_{Elements}\sum_{Gauss}\sqrt{\frac{2}{3}(\varepsilon_x^2+\varepsilon_z^2+\varepsilon_{xz}^2)}\right)^{1}}\right] \times 100 \leqslant Tol \quad (10)$$

where *Tol* is a prescribed convergence tolerance value. The subscript of the summation, *Gauss*, represents all gauss points of each element for numerical integral; the subscript *Elements* denotes all the element number of this 2D numerical model; ε_x, ε_z, and ε_{xz} are the total strain components. According to Owen and Hinton (1980), such a global measure for steady-state conditions (Eq. (10)) is superior to the measure at some selected points.

The above viscoelastic numerical models are applied to a hypothetical geological rock mass (Fig. 2a). The rock mass (domain) is 100 m high and 100 m wide and is discretized into 866 elements (i.e., the dimension of the refined grid is 2.5 m × 2.5 m, while the coarse grid is 5 m × 5 m), and 938 nodes. The cavern is 17.5 m in height and 15 m in width and located in the middle of the domain. The triangle symbols with or without circle represent mechanical boundary conditions (the same as Fig. A1 in Appendix A). Specifically, no displacement in the x-direction condition (i.e., $u_x = 0$) is assigned to the left-hand side and the right-hand site boundaries while the displacements of the domain bottom are set to be zero (i.e., $u_x = u_z = 0$.)

Before conducting the 2-D experiment, we verify the 2-D finite element program with the analytical solution for simulating a compression test (See Appendix A).

2.2. Reference fields

To numerically simulate the effects of heterogeneity and to test the ability of our back analysis algorithm, a synthetic heterogeneous rock mass is created (Fig. 2). As mentioned previously, geomechanical properties of geologic formations vary spatially (see Cai, 2011; Griffiths et al., 2009; Griffiths et al., 2011; Boyd et al., 2018). Therefore, the first elastic modulus (E_1), the viscidity coefficient (η_1), and the second elastic modulus (E_2) of the rock mass are treated as random fields; each field has its unconditional statistics (Yeh et al., 2015), representing its spatial variability. Table 1 lists the statistics, which are based on a comprehensive survey of published studies (Çanakci and Pala, 2007; Hsu and Nelson, 2006; Schweiger et al., 2001; Song et al., 2005; Song et al., 2011). Afterward, a Fast Fourier Transform (FFT) random field generator (Gutjahr, 1989) then assigns an E_1, η_1, and E_2 value to each element of the domain (Fig. 2b, 2c, and 2d) to create three heterogeneous parameter fields. Each field is generated with a different seed number such that each is independent of the other. These fields are the reference (or true) fields in the following analysis. Note that, since a variable grid is used, a random parameter field is generated based on

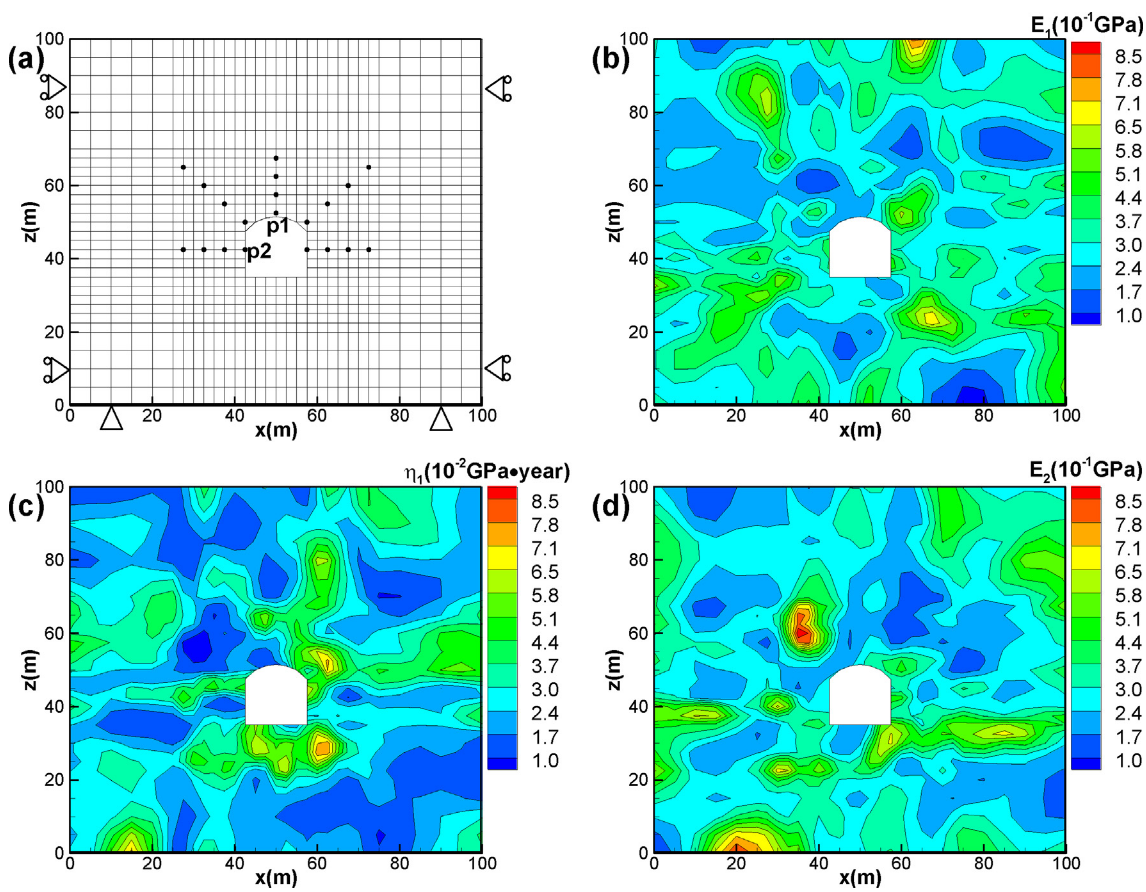

Fig. 2. (a) Mesh discretization of the FEM model and boundary conditions; heterogeneous (b) E_1, (c) η_1, (d) E_2 fields of the reference site.

Table 1
Unconditional statistics for each parameter.

Parameters	Values			
	Mean	Variance	*Cov(%)	correlation length, (m)
The first elastic modulus, E_1 (10^{-1}GPa)	3.0(1.0)	2.0(0.2)	47.1	$\lambda_x = \lambda_z = 10$
The viscidity coefficient, η_1(10^{-2}GPa■year)	2.58(0.8)	2.34(0.3)	59.3	$\lambda_x = \lambda_z = 10$
The second elastic modulus, E_2 (10^{-1}GPa)	3.0(1.0)	2.0(0.2)	47.1	$\lambda_x = \lambda_z = 10$

* Cov denote the coefficient of variation. () indicates the natural logarithm of each parameter.

the 2.5 m × 2.5 m grid for the whole domain, and then the parameter value of each coarse grid is the average of the parameter values of the fine grids within each coarse grid.

In the numerical experiments, we make the following assumptions:

1) The excavation does not alter in-situ rock properties. That is, the parameter field is assumed to be fixed in time and space during the excavation. This assumption may not be as realistic as it should be. It is, however, convenient for the following analysis since our knowledge of the metamorphosis of the parameter is limited. Moreover, our proposed inversion algorithm is not affected by this assumption since it relies on the observed displacement data and prior spatial statistics of the parameter only. In other words, as this approach is applied to a real-world situation, the estimated field reflects the metamorphosis of the parameter field due to excavation accordingly.
2) Poisson's ratio (υ) and unit weight (γ_g) are assumed to be constant since they have a negligible influence on the back analysis (Sakurai, 2017). Besides, because of the difficulty of determining the initial geostress, a reasonable and uniform value of the coefficient of lateral earth pressure (k_0) is assumed. All of these parameters used in the numerical simulation are listed in Table 2.

3. Effect of heterogeneity

Prior to the back analysis, we conduct forward simulations to investigate the displacement field and maximum shear strain field in the homogeneous and heterogeneous viscoelastic parameter fields after completion of the excavation of a URC. The purpose of this step is to demonstrate the effects of heterogeneity and their importance. In the following simulations, deformation and stability of a rock mass are evaluated using the maximum shear strain ($\gamma_{\max}$) (Sakurai, 1993; Sakurai, 2000;Sakurai, 2017):

$$\gamma_{\max} = |\varepsilon_1 - \varepsilon_3| \tag{11}$$

where ε_1 and ε_3 are the maximum and minimum principal strain, respectively. It should be noted that we apply only the KV constitutive model to conduct the forward simulations for explicating the effect of heterogeneity.

In the case of the homogeneous field, the viscoelastic parameter values of all elements are assigned a value that is equal to the mean of the heterogeneous parameter fields (i.e. $\mu_{E_1} = 3.0 \times 10^{-1}\,\text{GPa}$, $\mu_{\eta_1} = 2.58 \times 10^{-2}\,\text{GPa}$, and $\mu_{E_2} = 3.0 \times 10^{-1}\,\text{GPa}$, Table 1), and the other mechanical parameters, initial geostress condition, and boundary condition are the same as those for the heterogeneous case.

Table 2
Constant parameters for the viscoelastic numerical model.

Parameters	Values
Unit weight of granite, γ_g(KN/m^3)	25
Poisson's ratio, υ	0.3
coefficient of lateral earth pressure (k_0)	1.0
The convergence tolerance, *Tol*	0.2
The time interval, $\triangle t$(year)	0.0001

The displacements (u) at points p1 and p2 (Fig. 2a) for the homogeneous and the heterogeneous field are examined to represent the crown settlements and the sidewall expansion over time, respectively, as shown in Fig. 3a. Notice that the displacements of p1 and p2 for the homogeneous case are smaller than that of the heterogeneous case. Values of the ratio, Eq. (10), at each time step are illustrated as the dash-dotted lines in Fig. 3a before the convergence tolerance (i.e., $Tol = 0.2$ listed in Table 2) is reached. From the plot, we find that the deformation of the cavern in the case of heterogeneity takes a longer time to stabilize.

The spatial distributions of displacements near steady-state (i.e., t = 0.4 year) for the heterogeneous and the homogeneous case are shown in Fig. 3b and 3c, respectively. Overall, the distribution for the homogeneous case is symmetrical about the URC, while in the heterogeneous case, the displacements near the crown (red areas in Fig. 3b) are much larger than those at other places.

Likewise, the maximum shear strain ($\gamma_{\max}$) simulated using homogeneous E field is symmetrical (see Fig. 3e), while in the heterogeneous case, $\gamma_{\max}$ clusters at the left crown and the two floor-corners (see Fig. 3d), and the value is greater than that in the homogeneous case. These results indicate that neglecting the heterogeneity, one likely overestimates the stability of the cavern and underestimates the deformability, as well as miscalculates the stabilization time. That is, considering heterogeneity is important, and an effective method to characterize the spatial variability of these parameters is necessary for a reliable design and safe construction of URCs.

4. Back analysis method

To predict the deformation of a heterogeneous rock mass, we, therefore, propose to monitor the displacement using extensometers at early times after excavation, e.g., the period depicted as the red box in Fig. 3a. With these data, a back analysis then estimates E_1, η_1, and E_2 spatial distributions, which are used to forecast the displacements and the maximum shear strain distributions after excavation. The proposed approach provides a way to evaluate the stability of the cavern at later times and to design proper engineering mitigation measures if necessary.

A back analysis in this study is developed using a successive linear estimator (SLE) (Yeh et al., 1995; Yeh et al., 1996), which has been proven robust in hydraulic tomography analysis in hydrogeology field (Yeh and Liu, 2000; Liu et al., 2002; Illman et al., 2009; Xiang et al., 2009; Zhu and Yeh, 2005; Zha et al., 2014 and many others). Below is the description of the SLE algorithm tailored to our back analysis, and the procedure of this inverse approach is illustrated in Fig. 4.

Our back analysis first adopts the highly parameterized heterogeneous conceptual model (i.e., each element in the model has its parameter values). As such, we discretize the 2-D domain of the domain into N elements; each has three mechanical parameters (i.e., E_1, η_1, and E_2). These parameters are expressed in terms of their natural logarithm (i.e., $\ln E_1$, $\ln \eta_1$, and $\ln E_2$) to ensure the inversed parameter values are always positive.

The SLE considers these mechanical parameters as spatial random

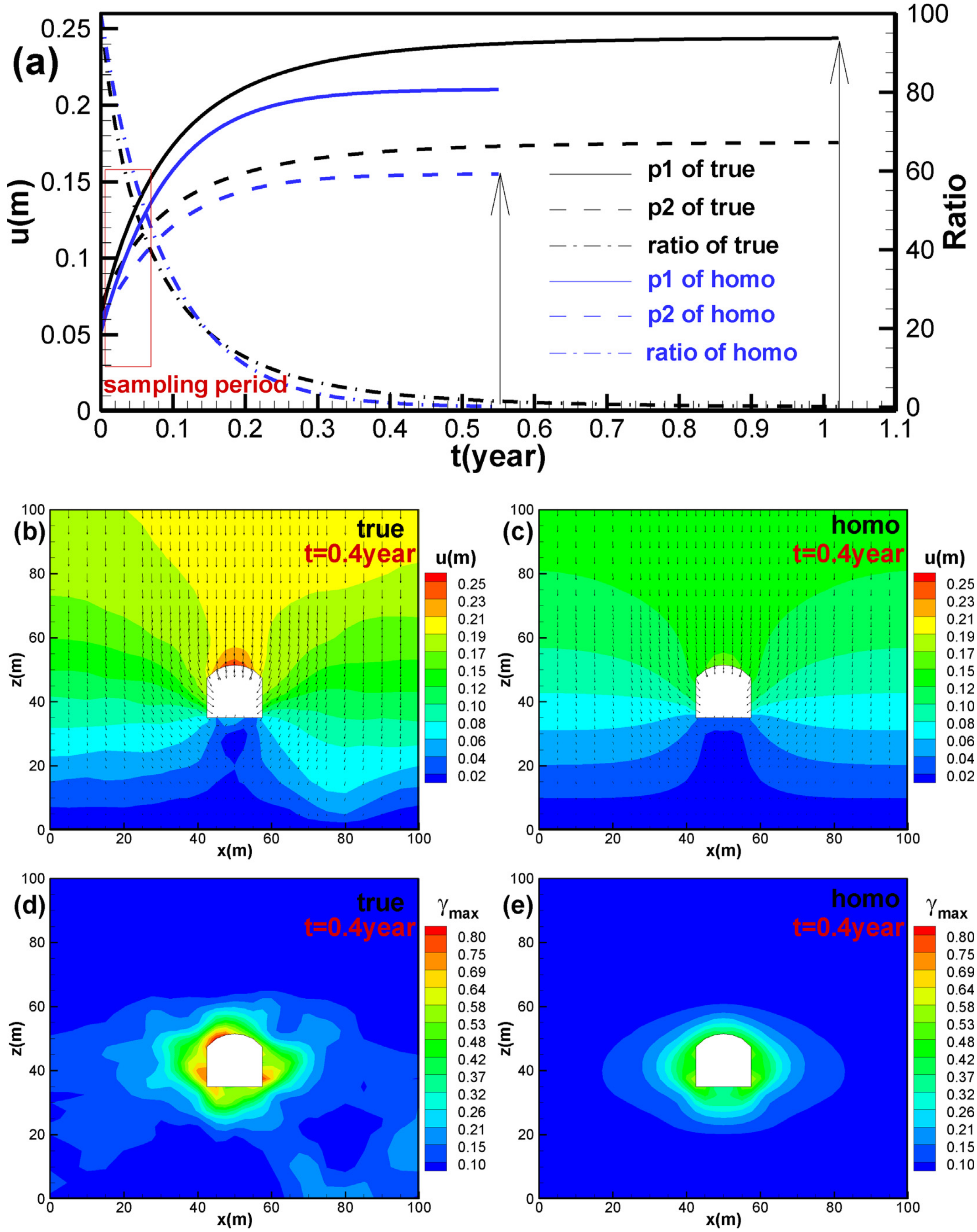

Fig. 3. (a) Simulated displacement behaviors at point p1 and p2 for the homogeneous and heterogeneous case; (b) the contour map of the displacement distribution at t = 0.4 year for the heterogeneous case; and (d) the contour map of the maximum shear strain for the heterogeneous case. For the homogeneous case, the corresponding plots are (c) and (e). The arrows are the displacement vectors.

fields, which are expressed as $\ln E_1(x) = A + a(x)$, $\ln \eta_1(x) = B + b(x)$, and $\ln E_2(x) = S + s(x)$. The A, B, and S are the unconditional means (i.e., $A = \langle \ln E_1(\mathbf{x})\rangle$, $B = \langle \ln \eta_1(\mathbf{x})\rangle$, $S = \langle \ln E_2(\mathbf{x})\rangle$, the angle bracket denotes the expected value); $a(x)$, $b(x)$, and $s(x)$ are the unconditional perturbations with a zero mean ($\langle a(\mathbf{x})\rangle = 0$, $\langle b(\mathbf{x})\rangle = 0$, and $\langle s(\mathbf{x})\rangle = 0$). The word "unconditional" means that no sampled parameter values or displacement data are used to constraint the means or perturbations. An exponential spatial covariance function characterizes the relationship between perturbations of a given parameter in the two-dimensional domain:

$$R_{aa}(P, P') = \sigma_a^2 \exp[-\sqrt{(x-x')^2/\lambda_x^2 + (z-z')^2/\lambda_z^2}] \tag{12}$$

$$R_{bb}(P, P') = \sigma_b^2 \exp[-\sqrt{(x-x')^2/\lambda_x^2 + (z-z')^2/\lambda_z^2}] \tag{13}$$

$$R_{ss}(P, P') = \sigma_s^2 \exp[-\sqrt{(x-x')^2/\lambda_x^2 + (z-z')^2/\lambda_z^2}] \tag{14}$$

That is, the relationship of the viscoelastic properties at the point $P(x, z)$ and the point $P'(x', z')$ decreases as the separation distance between the two points increases. In Eqs. (12), (13), and (14), σ_a^2, σ_b^2 and σ_s^2 denote the variance of $\ln E_1$, $\ln \eta_1$, and $\ln E_2$, respectively; λ_x and λ_z, are the correlation scales in x and z directions, respectively, and they are assumed to be the same for the three properties (see Table 1). Physically, the correlation scale dictates that any pair of viscoelastic values located within the correlation scales must have similar values to reflect the fact that they are in the same geologic unit. It, therefore,

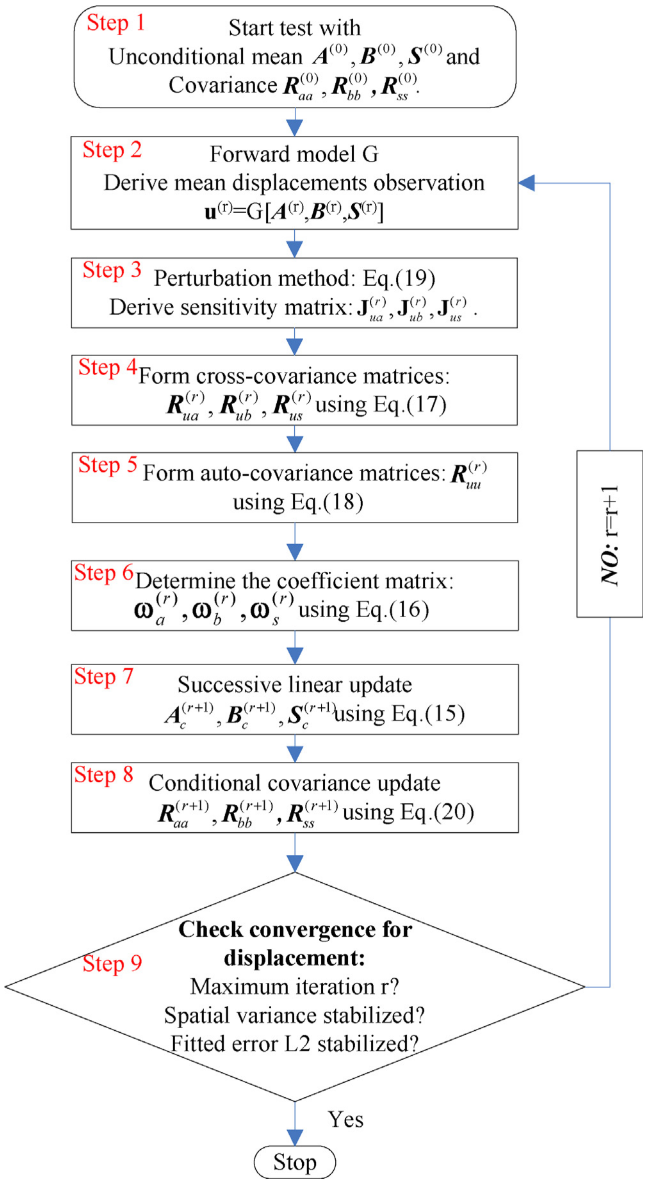

Fig. 4. Flowchart of the proposed back analysis approach.

could be regarded as the overall fabric of the geologic medium (i.e., average length, thickness, and width of heterogeneity at a field site) (Yeh et al., 2015).

SLE aims to derive the statistically most likely estimate of the parameter value (i.e., conditional expectation) for each element, given (conditioned with) the observed displacement data from extensometers. Also, the estimated parameter fields could predict the most likely deformation behaviors of the rock mass, given the observed displacements.

The SLE starts with some prior knowledge about the mean values of the unknown $\ln E_1$, $\ln \eta_1$, and $\ln E_2$ parameter fields, which are represented as parameter vectors, $A(N\times1)$, $B(N\times1)$, and $S(N\times1)$ in the numerical model, respectively. In addition to the mean value, SLE also assumes that the unknown parameter fields possess the spatial covariances (Eqs. (12), (13), and (14)), $R_{aa}(N \times N)$, $R_{bb}(N \times N)$, and $R_{ss}(N \times N)$ hereafter. These mean and covariance are called unconditional mean and covariance.

Suppose we install extensometers at n_p observation locations and collect displacements at n_t different times. The total number of observed displacements, n_u, is $n_p \times n_t$, denoted as $\mathbf{u}^*$, a $n_u \times 1$ data vector. Then, the estimated parameter vectors, conditioned by the observations, are A_c, B_c, and S_c (subscript c denotes conditional), which are iteratively determined using the stochastic linear estimator:

$$A_c^{(r+1)} = A_c^{(r)} + \omega_a^T(\mathbf{u}^* - G(A_c^{(r)}, B_c^{(r)}, S_c^{(r)})),$$
$$B_c^{(r+1)} = B_c^{(r)} + \omega_b^T(\mathbf{u}^* - G(A_c^{(r)}, B_c^{(r)}, S_c^{(r)})),$$
$$S_c^{(r+1)} = S_c^{(r)} + \omega_s^T(\mathbf{u}^* - G(A_c^{(r)}, B_c^{(r)}, S_c^{(r)})). \tag{15}$$

where r is the iteration index; $\mathbf{G}(.)$ is the forward numerical model (Section 2.1), which simulates displacements at the observation locations using the parameters at iteration r, i.e., $A_c^{(r)}$, $B_c^{(r)}$, and $S_c^{(r)}$. Note that when $r = 0$, $A_c^{(0)} = A$, $B_c^{(0)} = B$, and $S_c^{(0)} = S$ (unconditional mean values). Since the relationship between the parameters and $\mathbf{u}$ is nonlinear, the linear estimator (Eq. (15)) is used iteratively to exploit the information content about AB, and S in the observed data $\mathbf{u}$. In Eq. (15), the coefficient matrixes, $\omega_a(n_u \times N)$, $\omega_b(n_u \times N)$, and $\omega_s(n_u \times N)$ are the weights, which assign the contribution of the difference between the observed and simulated displacements at each observation location to previously estimated parameter value at each element. The superscript T denotes the transpose.

The coefficient matrix, ω_a, ω_b, and ω_s, are determined by solving the following equation:

$$[R_{uu}^{(r)} + \theta^{(r)}\mathrm{diag}(R_{uu}^{(r)})]\omega_a^{(r)} = R_{ua}^{(r)},$$
$$[R_{uu}^{(r)} + \theta^{(r)}\mathrm{diag}(R_{uu}^{(r)})]\omega_b^{(r)} = R_{ub}^{(r)},$$
$$[R_{uu}^{(r)} + \theta^{(r)}\mathrm{diag}(R_{uu}^{(r)})]\omega_s^{(r)} = R_{us}^{(r)}. \tag{16}$$

where $R_{uu}^{(r)}$ is the auto-covariance of observation data. $R_{ua}^{(r)}$, $R_{ub}^{(r)}$, and $R_{us}^{(r)}$ are the cross-covariance between the parameters and data. The parameter θ is a dynamic stability multiplier, and $\mathrm{diag}(R_{uu}^{(r)})$ is a stability matrix, which contains diagonal components of $R_{uu}^{(r)}$. Therefore, the solution to Eq. (16) requires the knowledge of auto-covariance $R_{uu}^{(r)}$ and cross-covariance $R_{ua}^{(r)}$, $R_{ub}^{(r)}$, and $R_{us}^{(r)}$ at each iteration, r. These covariances are calculated using the first-order numerical approximation:

$$R_{ua}^{(r)} = \mathbf{J}_{ua}^{(r)}R_{aa}^{(r)},$$
$$R_{ub}^{(r)} = \mathbf{J}_{ub}^{(r)}R_{bb}^{(r)},$$
$$R_{us}^{(r)} = \mathbf{J}_{us}^{(r)}R_{ss}^{(r)}. \tag{17}$$

$$R_{uu}^{(r)} = \mathbf{J}_{ua}^{(r)}R_{aa}^{(r)}\mathbf{J}_{ua}^{(r)\mathrm{T}} + \mathbf{J}_{ub}^{(r)}R_{bb}^{(r)}\mathbf{J}_{ub}^{(r)\mathrm{T}} + \mathbf{J}_{us}^{(r)}R_{ss}^{(r)}\mathbf{J}_{us}^{(r)\mathrm{T}} \tag{18}$$

At iteration $r = 0$, $R_{aa}^{(0)}$, $R_{bb}^{(0)}$, and $R_{ss}^{(0)}$ in Eqs. (17) and (18) are the unconditional covariance of parameters. $J_{ua}^{(r)}(n_u \times N)$, $J_{ub}^{(r)}(n_u \times N)$, and $J_{us}^{(r)}(n_u \times N)$ are the sensitivity (Jacobian) matrix of displacement at each observation location at a given time with respect to the parameter at each element, and are evaluated using the parameters estimated at the current iteration. These sensitivity matrices are determined by a perturbation approach. Specifically, the approach solves the forward model for $\mathbf{u}$ at the observation location and time, based on the parameter fields estimated at current iteration ($A_c^{(r)}$, $B_c^{(r)}$, and $S_c^{(r)}$). It then solves for another $\mathbf{u}$ with some perturbed values (i.e., $A_c^{(r)} + \Delta A_i$, $B_c^{(r)} + \Delta B_i$, and $S_c^{(r)} + \Delta S_i$, $i = 1,2, \ldots, N$). Then, a first-order numerical approximate of the state sensitivity is used:

$$J_{ua}^{(r)} = \frac{\partial u}{\partial A} = \frac{\Delta u}{\Delta A_i} = \frac{u_{A_c^{(r)}+\Delta A_i} - u_{A_c^{(r)}}}{\Delta A_i},$$
$$J_{ub}^{(r)} = \frac{\partial u}{\partial B} = \frac{\Delta u}{\Delta B_i} = \frac{u_{B_c^{(r)}+\Delta B_i} - u_{B_c^{(r)}}}{\Delta B_i},$$
$$J_{us}^{(r)} = \frac{\partial u}{\partial S} = \frac{\Delta u}{\Delta S_i} = \frac{u_{S_c^{(r)}+\Delta S_i} - u_{S_c^{(r)}}}{\Delta S_i}. \tag{19}$$

The sensitivity analysis during each iteration is carried out as follows. The forward model $\mathbf{G}(.)$ first simulates the base-line mean displacement fields at n_t sampling times with the given mean values of the three parameters (i.e., corresponding to the step 2 of the flowchart in Fig. 4). $\mathbf{G}(.)$ is then solved for the displacement fields over the sampling times with a given perturbed parameter value at element i. Since the effect of the perturbed values of the three parameters at every element, ΔA_i, ΔB_i, and ΔS_i, must be evaluated, we must solve $\mathbf{G}(.)$ 3 N times, where N is the total number of elements in the domain. Afterward, sensitivities at observed locations for the three parameters at each element at the observation times are derived from Eq. (19). The above procedure is repeated for each iteration. During each iteration, the base-line and perturbed displacement fields are evaluated with newly estimated conditional mean parameter fields. This perturbation approach could be computationally expensive if the number of elements, where parameters are to be determined, is huge. Alternatively, the sensitivity can be derived using an adjoint approach (see Sykes et al., 1985; Grégoire et al., 2004).

For $r \geq 1$ the covariance function is updated to obtain the conditional covariance of the parameter according to

$$\begin{aligned} R_{aa}^{(r+1)} &= R_{aa}^{(r)} - \omega_a^T R_{ua}^{(r)}, \\ R_{bb}^{(r+1)} &= R_{bb}^{(r)} - \omega_b^T R_{ub}^{(r)}, \\ R_{ss}^{(r+1)} &= R_{ss}^{(r)} - \omega_s^T R_{us}^{(r)}. \end{aligned} \tag{20}$$

This update is to reflect the improvement (i.e., reduction of the uncertainty) on the estimate due to the iterative extraction of heterogeneity information from the measured displacement data.

Three convergence criteria to terminate the iteration are considered: (1) The change in the spatial variance of the estimated parameter field between current and last iterations is smaller than a specified tolerance, implying that the SLE cannot improve the estimation any further. (2) The change of simulated displacements between successive iterations is smaller than a given tolerance, indicating that the estimates will not significantly improve the displacements field. (3) The maximum iteration reaches the given number. If one of the three criteria is met, the iteration ceases, and the estimates are e optimal.

In this application of SLE, Variably Saturated Flow and Transport in 2D (VSAFT2), a finite element numerical model code for simulating both forward and inverse aquifer problem (available at www.hwr.arizona.edu/yeh), by Yeh et al. (1993), is modified to accommodate our mechanical inverse problem. That is, in order to adapt VSAFT2 for our study, the hydrology forward model is replaced by the viscoelastic mechanical forward model provided, and the sensitivity calculation method used in VSAFT2 is also replaced by the perturbation method (i.e., Eq. (19)).

5. Numerical experiments

In the following numerical experiments, we assume that the deformation of the URC with time in the reference field follows the KV model. Thereby, the observed displacements for the inversion are derived from the forward simulation based on the KV model with the corresponding heterogeneous parameters in Fig. 2b, 2c, and 2d. After completing the excavation, the simulated nodal displacements at the 20 observation locations (see black dots in Fig. 2a) and at the time 0.01, 0.03, 0.05, and 0.07 years (within the red box shown in Fig. 3a) are collected, i.e., the total number of observed displacement data is 80.

As mentioned previously, the KV model and the PT model have been proposed for the viscous strain and stress relationship for simulating the time-dependent behaviors of the rock mass. We, therefore, investigate two cases: Case 1, a consistent viscoelastic constitutive model (KV) is used for the forward simulation as well as back analysis. Case 2, the PT model is used in the inversion of the responses derived from the KV model.

5.1. Case 1. (Consistent VCM)

With the sparsely sampled displacements, E_1, η_1, and E_2 fields are simultaneously estimated using SLE, and the estimates are displayed in Fig. 5a, 5b, and 5c, respectively. The estimated fields near the displacement sampling locations resemble the true parameter fields (Fig. 2b, 2c, and 2d), while the estimated fields in the coarse region (away from the sampling locations) are much smoother than the reference fields. Notice that an abnormal area appears below the cavern floor (red dashed box in Fig. 5a and 5c), i.e., the estimated E_1 and E_2 fields of this area is larger than the reference field. The result is likely owing to the insufficient data near this region for the inverse analysis.

Comparing the estimated η_1 and E_2 fields, we notice that the resolution of the estimated E_1 field (Fig. 5a) is low. The physical meaning of the KV model explains this low-resolution result. Since the spring represented by E_1 is connected parallel to the dashpot represented by η_1(see Fig. 1a), a small movement of the dashpot in a short time after loads are applied, leads to that the E_1 spring does not fully use its elastic property and play a role in the deformation. Besides, our displacement sampling is taken at early times after excavation. For this reason, the estimated E_1 field is identifiable only at low-resolution by the displacement response.

To compare the estimation errors, we plot the histograms of the true and estimated fields of the three parameters in Fig. 5d, 5e, and 5f, along with their spatial mean and variance, which are defined as

$$\mu = \left(\sum_{j=1}^{N} Z_j\right) \Big/ N \text{ and } Var = \left[\sum_{j=1}^{N} (Z_j - \mu)\right]^2 \Big/ N \tag{21}$$

where Z_j stands for the true or estimated $\ln E_1$, $\ln \eta_1$, and $\ln E_2$, respectively; j indicates the element number, and N is the total number of elements. From these histograms, we observe that the true and estimate parameters are normally distributed, and the spatial mean of the estimated $\ln E_1$, $\ln \eta_1$, and $\ln E_2$ are almost equal to the reference fields, indicating estimates distributions are statistically unbiased in comparison with the reference. The spatial variance of the estimated $\ln E_1$ is smaller than that of $\ln \eta_1$, and $\ln E_2$. Thus, it agrees with the low resolution of the estimated E_1 field as mentioned before.

Contour plots of the conditional variances (the diagonal term of $R_{aa}^{(r+1)}$, $R_{bb}^{(r+1)}$, and $R_{ss}^{(r+1)}$ at the final iteration step), which represent the uncertainty of the estimate at each location, for the estimated $\ln E_1$, $\ln \eta_1$, and $\ln E_2$ fields are displayed in Fig. 5g, 5 h, and 5i, respectively. The conditional variances of these fields near the observation positions are small, while they are relatively large far away from the observation ports, especially near the boundary. More importantly, the uncertainty around the cavern is the smallest, indicative of high confidence in the estimates around the cavern, which is critical in assessing the deformability and stability of the surrounding rock masses.

5.2. Case 2 (inconsistent VCM)

The estimated results based on the PT model and the observed displacements from the forward simulation based on KV model are shown in Fig. 6. A glance of the estimated E_1, η_1, and E_2 fields (see Fig. 6a, 6b, and 6c) reveals that the estimated fields are relatively smaller than the reference fields (Fig. 2b, 2c, and 2d). According to Fig. 6d, 6e, and 6f, estimates, and true parameter histograms are normally distributed, and, to some extent, the centers of the histograms of estimated parameters are smaller than those the true field, especially for η_1 and E_2 fields. This finding indicates that estimates distributions are biased. As mentioned in the previous section, at the beginning period after the excavation completion, the displacements of the cavern with the KV model are dominated by the instantaneous elastic deformation (i.e., $\sigma_c/E_2{}^{KV}$ in Fig. 1a). While the displacement of the cavern with the PT model at the early times is mainly determined by $\sigma_c/(E_1 + E_2)^{PT}$ (Fig. 1b). Because of this reason, to make the simulated displacements agree with the observed, SLE adjusts E_1 and E_2 values to smaller values when the PT model is used in the back analysis.

Besides, based on the physical meaning of η_1 (i.e., a measure of the viscidity of fluid material), the smaller η_1 value of a material is, the faster deformation reaches the steady-state. As illustrated in Fig. A2 of Appendix A, the displacement with KV model is significantly faster than that of PT model to reach a steady state. Thus, the η_1 value in the PT model has to be smaller in order to obtain a similar rate of deformation.

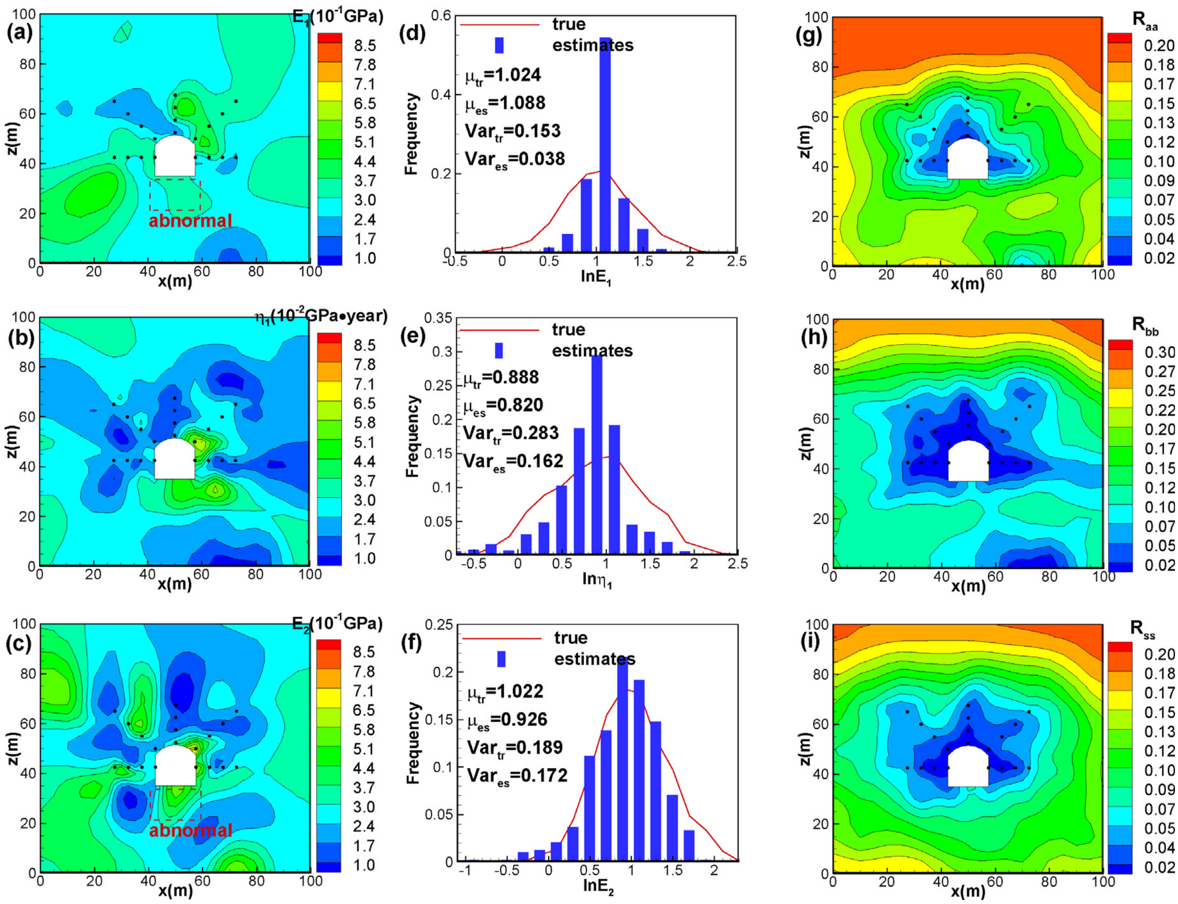

Fig. 5. Back analysis results with the consistent viscoelastic constitutive model (VCM): estimated (a) E_1, (b) η_1, (c) E_2 field; the histogram of estimated versus true fields for (d) $\ln E_1$, (e) $\ln \eta_1$, (f) $\ln E_2$; the associated conditional variances of (g) $\ln E_1$, (h) $\ln \eta_1$, (i) $\ln E_2$. μ_{tr} and Var_{tr} represent the spatial mean and spatial variance of the true fields, respectively, and the μ_{es} and Var_{es} represent that of estimated fields.

The uncertainty of the estimated E_1, η_1, and E_2 fields are displayed in Fig. 6g, 6h, and 6i, respectively. These uncertainties (i.e., conditional variances) near the observation positions are small, while they are relatively large far away from the observation locations, especially near the upper boundary.

The scatterplots of the simulated displacements versus the observed at different times for these two cases are prepared in Fig. 7a and 7b, respectively. A linear model is fitted to the scatter data without forcing the intercept to zero. The simulated displacements from the final estimated parameters field and the observed are in good agreement (the blue dots in these figures). Since there are no measurement errors or noises, the slope and R^2 are nearly equal to unity in both of two cases at the final iteration, and the magnitudes of L1 and L2 are small: 10^{-4} (m) and 10^{-7} (m^2) for the case of using consistent VCM, 10^{-3} (m) and 10^{-6} (m^2) for the case of using inconsistent VCM, respectively. These plots show that our calibration efforts are adequate, even using inconsistent VCM. More importantly, Figs. 5–7 demonstrate that matching the simulated and observed displacements satisfactorily does not guarantee the accurate estimates of parameter fields.

6. Assessment of inversion results

6.1. Validation

The final goal of any site characterization is to provide an accurate prediction of displacements or stability at critical locations of a URC. For this reason, a rationale means for validating these estimates is to simulate displacements at various locations, where no data are used in the inversion, and to check the accuracy of the predicted displacements. We thereby utilize the estimated parameters obtained from the SLE with consistent VCM (Fig. 5a, 5b, and 5c) and with the inconsistent VCM (Fig. 6a, 6b, 6c) to simulate displacements of the cavern periphery at the different times (t = 0.01, t = 0.1, and t = 0.4 years).

Predicted displacements at 19 locations along the periphery are displayed from an A-B-C-D clock-wise order, as illustrated in Fig. 8. In general, both of the estimates using the consistent and the inconsistent VCM predict a similar pattern of the displacements as the true displacements. At the early and the intermediate times (i.e., t = 0.01 and t = 0.1 year, respectively), the parameter fields estimated with consistent VCM result in better predictions of the displacements than using the parameter fields estimated with inconsistent VCM. Nevertheless, at the latter time (i.e., t = 0.4 year), the displacements using the estimates with the consistent VCM are under-predicted the true displacements. This underestimation is likely because only displacements observations at early times and sparse locations are used for inversion.

Generally, the maximum shear strain (γ_{max}) reflects the stability state of the cavern and is an appropriate indicator for the potentially unstable zone of the surrounding rock masses. For this reason, γ_{max} distributions at late times based on the estimates using the consistent and the inconsistent VCM are illustrated in Fig. 9a and b, respectively. They show that γ_{max} distributions based on both estimates yield high-value zones at the left crown and the two corners of the floor of the cavern consistent with the true γ_{max} distribution (see Fig. 3d). The scatter plots showing predicted maximum shear strains vs. the true ones over the entire domain are presented in Fig. 9c and 9d. The red circles are the predicted and the true shear strain pairs within the red rectangle in Fig. 9a and 9b, which is the region of our concern. While the predicted γ_{max} values are not exact but unbiased, even though the estimated

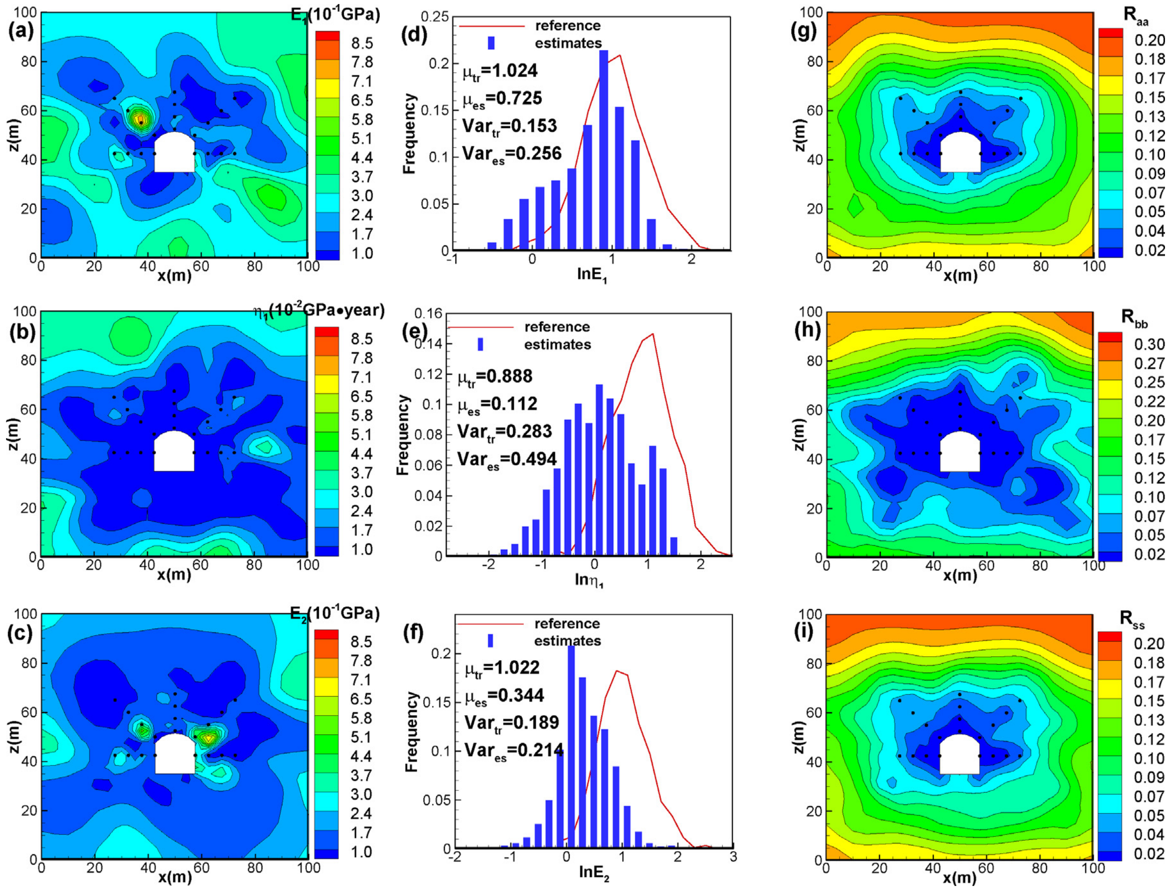

Fig. 6. Back analysis results with the inconsistent viscoelastic constitutive model (VCM): estimated (a) E_1, (b) η_1, (c) E_2 field; the histogram of estimated versus true fields for (d) $\ln E_1$, (e) $\ln \eta_1$, (f) $\ln E_2$; the associated conditional variances of (g) $\ln E_1$, (h) $\ln \eta_1$, (i) $\ln E_2$. μ_{tr} and Var_{tr} represent the spatial mean and spatial variance of the true fields, respectively, and the μ_{es} and Var_{es} represent that of estimated fields.

parameter fields with inconsistent VCM are biased, as mentioned in Section 5.2. However, the predicted values from the inconsistent VCM scatter slightly larger than those with consistent VCM. The result is exciting: using the estimated parameter field derived from SLE, one can derive an excellent prediction of the displacements and unstable-zone behavior so long some displacement and prior geostatistics information are available.

6.2. Uncertainty of prediction

Due to our limited ability to fully characterize the spatial variability of the parameters, our estimated parameters and predicted responses are subjected to uncertainty. To evaluate the uncertainty, the predicted vertical displacement at point p1 (u_y) and the horizontal displacement (u_x) at point p2 with upper-bound and lower-bounds, which denote the predicted displacement plus/minus the standard deviations of the displacements (σ_{u_x} and σ_{u_y}).

As discussed previously, the SLE aims to derive the conditional mean fields, which could predict the most likely (i.e., minimum uncertain) spatiotemporal evolution of the displacement, with given observed datasets. To reinforce this point, we compare the predicted evolution of the displacements and their uncertainty based on the

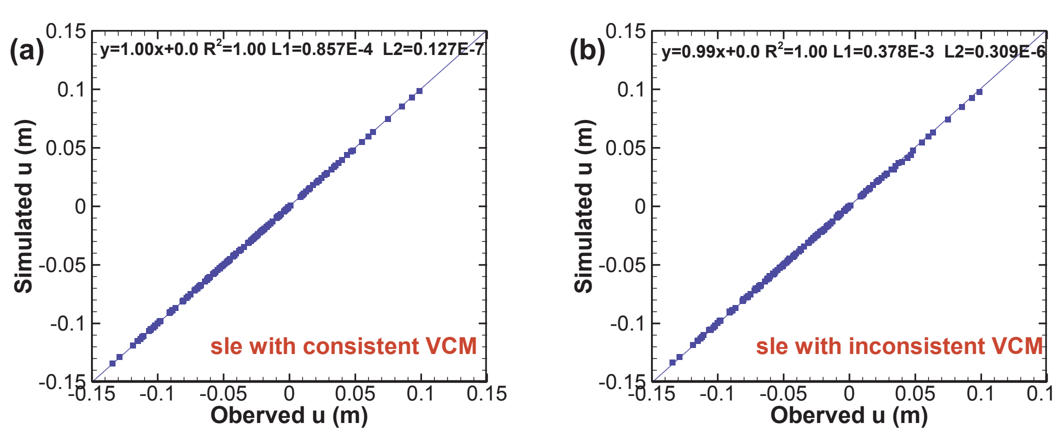

Fig. 7. The scatterplots of simulated versus observed displacements at the final iterations for (a) SLE with consistent VCM, (b) SLE with inconsistent VCM, illustrating calibration results.

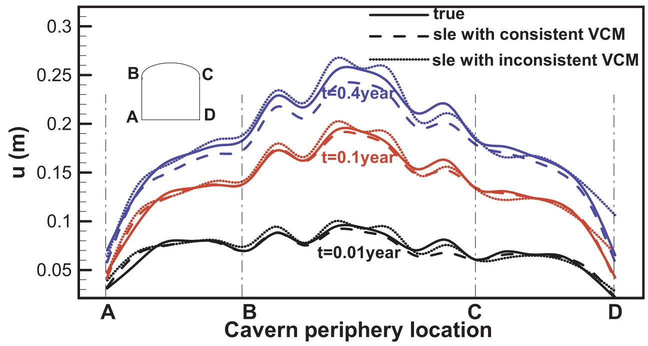

Fig. 8. Validation results of the predicted displacements of the cavern periphery at different times based on the SLE estimated parameter fields.

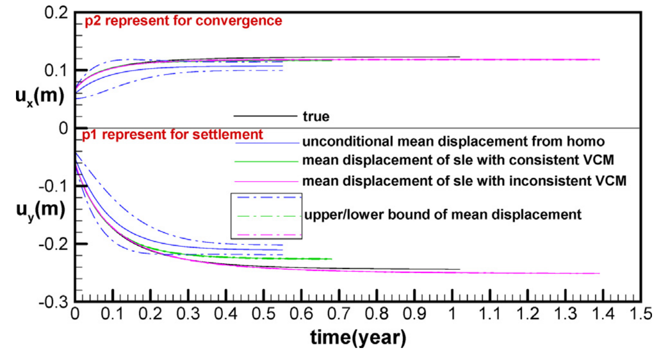

Fig. 10. Comparison of displacements and its uncertainty at point p1 and p2 predicted based on SLE estimated field with consistent VCM and inconsistent VCM.

conditionally estimated parameter fields and unconditional (homogeneous) parameter fields. The unconditional and conditional standard deviations (uncertainty), σ_{u_x} and σ_{u_y}, are determined by a first-order approximation to avoid tedious Monte Carlo simulations:

$$R_{u_x u_x} = \mathbf{J}_{u_x a} R_{aa} \mathbf{J}_{u_x a}^{\mathrm{T}} + \mathbf{J}_{u_x b} R_{bb} \mathbf{J}_{u_x b}^{\mathrm{T}} + \mathbf{J}_{u_x s} R_{ss} \mathbf{J}_{u_x s}^{\mathrm{T}}$$
$$R_{u_y u_y} = \mathbf{J}_{u_y a} R_{aa} \mathbf{J}_{u_y a}^{\mathrm{T}} + \mathbf{J}_{u_y b} R_{bb} \mathbf{J}_{u_y b}^{\mathrm{T}} + \mathbf{J}_{u_y s} R_{ss} \mathbf{J}_{u_y s}^{\mathrm{T}} \tag{22}$$

where the diagonal term of $R_{u_x u_x}(N_t \times N_t)$ and $R_{u_y u_y}$ $(N_t \times N_t)$ are the variance of u_x at point p2 and that of u_y at point p1. Taking the square root of the diagonal term produces the σ_{u_x} and σ_{u_y} at every time steps (N_t) of the entire period after excavation. $J(N_t \times N)$ is the sensitivity (Jacobian) matrix of displacement with respect to each element. N is the total number of elements in our finite element model. For unconditional cases, R_{aa}, R_{bb}, and R_{ss} are the unconditional parameter covariances, and $\mathbf{J}$ is evaluated at the unconditional mean parameters. Meanwhile, for the conditional cases, R_{aa}, R_{bb}, and R_{ss} are the conditional covariances from Eq. (20) at the last iteration, and $\mathbf{J}$ is evaluated at the conditional mean parameters.

Fig. 10 shows the predictions based on the unconditional approach (the solid blue line) and the conditional approach (the solid green line and the solid pink line). The conditional upper/lower bounds of predicted displacements at p1 and p2 points are much smaller than those of the unconditional case. That is, the conditional approaches give us high confidence for the assessment of displacement evolution of the cavern. Thus, if the mean parameter values are used only in the displacement prediction, the predicted displacement has high uncertainty. In contrast, a fusion of displacement measurements in the back analysis

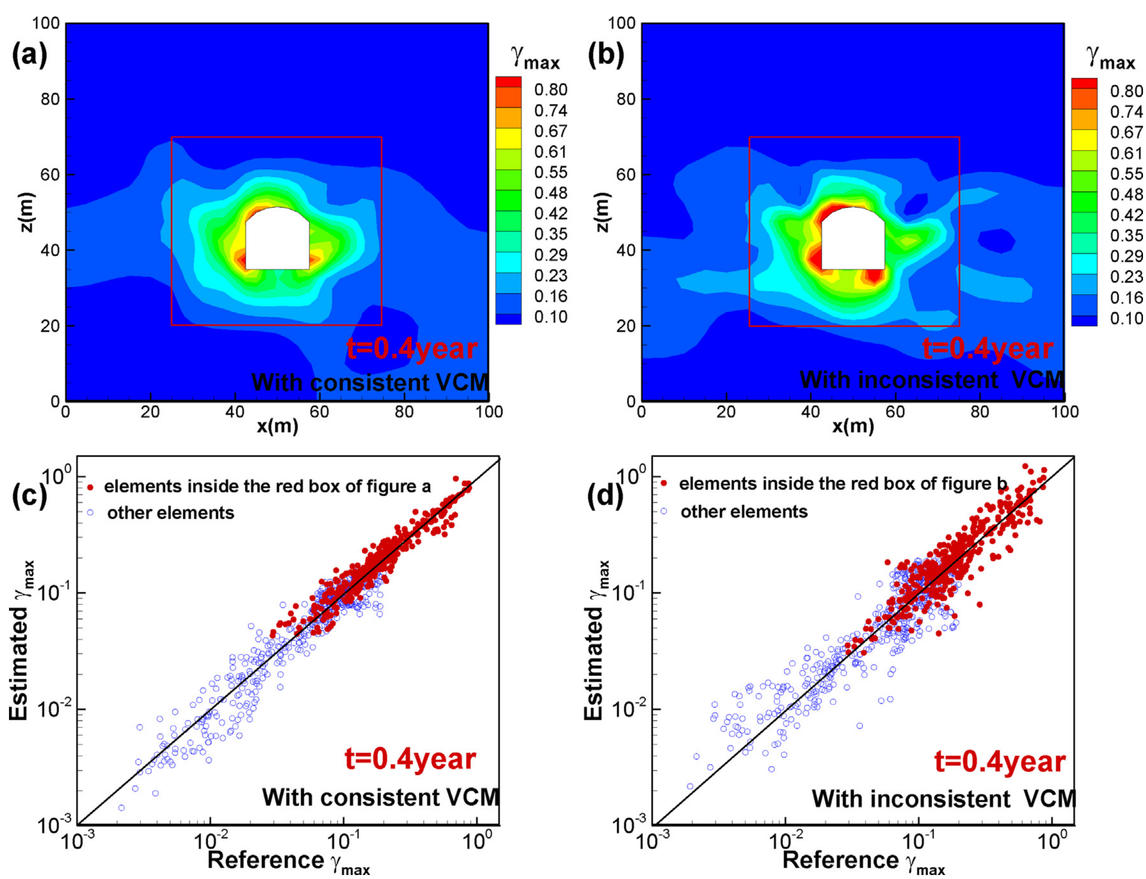

Fig. 9. Validation results of the contour map of maximum shear strain for (a) SLE with consistent VCM, (b) SLE with inconsistent VCM; (c) and (d) the scatter plots showing predicted maximum shear strain vs. the true over the entire domain. The red circles are the comparison of the predicted maximum shear strain and the true within the red rectangle in (a) and (b). (For interpretation of the references to colour in this figure legend, the reader is referred to the web version of this article.)

decreases the uncertainty and leads to a realistic assessment of the deformation of the cavern.

7. Conclusions

We develop a stochastic successive linear estimator (SLE) algorithm for simultaneously estimating the spatially varying viscoelastic parameter fields (i.e., viscidity coefficient and two different elastic moduli) after the excavation of an unlined rock carven (URC) in a heterogeneous rock mass. Based on synthetic cases, we show that the inversion algorithm is a promising and viable tool for mapping detailed spatial variation of the viscoelastic parameters, using only a limited number of extensometer data after completion of the cavern. We also demonstrate that the resolutions of the first elastic modulus (E_1) of the KV model is lower than the viscidity coefficient (η_1) and the other elastic modulus (E_2), due to the use of observed displacements sampling at the early period. Even so, they are sufficient to yield satisfactory predictions of the displacements and high maximum shear strain zone around the cavern.

In addition, if an inconsistent viscoelastic constitutive model is used for the SLE inversion, the estimated mechanical model parameters also could be adequately calibrated and could satisfactorily predict deformation and unstable-zone of a cavern. Overall, the SLE algorithm is a robust and useful tool.

More importantly, the SLE analysis provides the uncertainty estimate associated with the estimated parameter fields under available information. This uncertainty could serve as a guide for possible engineering reinforcement.

While we believe that these results are exciting, we acknowledge that they are based on numerical experiments, in which data noise and excavation disturbances are excluded. Therefore, the approach needs more applications to field problems. Moreover, only two different viscoelastic constitutive models are assumed, and three parameters are identified in this back analysis. To fully evaluate the time-dependent features of the plastic zone during the construction of URC, an elastic-viscoplastic constitutive model should be adopted, and a back analysis for determining the material strength parameters (e.g., the cohesion and the internal friction angle) should be developed.

CRediT authorship contribution statement

Xu Gao: Conceptualization, Writing - original draft, Formal analysis. **E-Chuan Yan:** Validation, Supervision. **Tian-Chyi Jim Yeh:** Methodology, Software, Writing-review & editing. **Xiao-Meng Yin:** Validation, Visualization. **Jing-Sen Cai:** Software, Validation. **Yong-Hong Hao:** Supervision. **Jet-Chau Wen:** Writing-review & editing.

Declaration of Competing Interest

The authors declare that they have no known competing financial interests or personal relationships that could have appeared to influence the work reported in this paper.

Acknowledgements

The first author acknowledge the support by the Fundamental Research Funds for the Central Universities, China University of Geosciences (Wuhan) (Grant No. G1323520270) and Engineering Research Center of Rock-Soil Drilling & Excavation and Protection, Ministry of Education. The second author acknowledge the support by the National Natural Science Foundation of China (Grant No. 41672313). The fourth author acknowledge the support by the National Natural Science Foundation of China (Grant No. 41807240). The fifth author acknowledge the support by the National Natural Science Foundation of China (Grant No. 41807264), and the Fundamental Research Funds for the Central Universities, China University of Geosciences (Wuhan) (Grant No. CUG170686). The corresponding author acknowledges the partially supported by the U.S. NSF grant EAR1931756.

Appendix A

The example considered here is the viscoelastic deformation of one-dimensional rock column with 10 elements under a constant loading (Fig. A1). The dimension of each element is 1 m × 1 m and the applied load is 3.2 MPa. The assumed material properties are included in Fig. A1, where it is noted that the unit weight and Poisson's ratio are taken to be zero. It means that the self-weight of the column is neglected and the 2-D finite element mechanical numerical code is transformed to simulate the 1-D problem. After given the time interval and the convergence tolerance as $\triangle t = 0.0001$ year and $Tol = 0.2$, respectively, the numerical solutions of the compression displacement (i.e., u_y) for the two constitutive models are illustrated in Fig. A2.

For comparison, the analytical solution of this 1-D problem based on the KV model is (Paraskevopoulou and Diederichs, 2018; Yang et al., 2001)

$$u_y = \frac{\sigma_c}{E_2} + \frac{\sigma_c}{E_1}\left(1 - e^{-\frac{E_1 t}{\eta_1}}\right) \tag{A1}$$

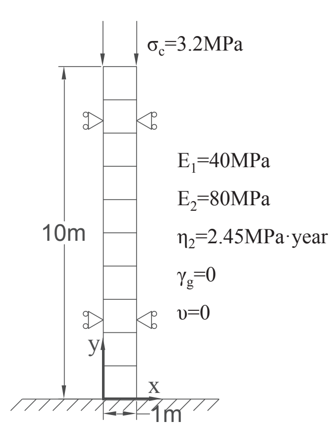

Fig. A1. Mesh discretization of the FEM model for one-dimensional problem and boundary conditions and associated parameters used in this problem.

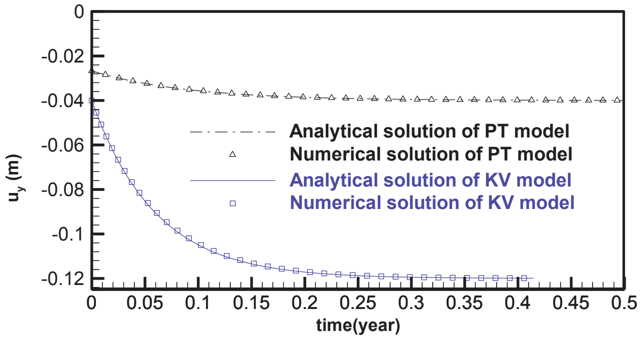

Fig. A2. Comparison of analytical and numerical solution of the one-dimensional compression problem based on Kelvin-Voigt (KV) model and Poynting-Thomson (PT) model.

While the analytical solution of this 1-D problem based on the PT model is

$$u_y = \frac{\sigma_c}{E_2}\left(1 - \frac{E_1}{E_1 + E_2} e^{-\frac{E_1 E_2 t}{(E_1 + E_2)\eta_1}}\right) \tag{A2}$$

Based on the same time interval, the analytical solutions of u_y are also shown in Fig. A2. As expressed in Eqs. (A1) and (A2), at the instantaneous moment of applying the load (i.e., t = 0), the displacement of the column for KV model and the PT model are equal to σ_c/E_2 and $\sigma_c/(E_1 + E_2)$, respectively; when the time tends to infinity (i.e., t → ∞), the u_y for KV model and the PT model are equal to $\sigma_c(E_1 + E_2)/(E_1E_2)$ and σ_c/E_2, respectively. From the comparison of the u_y curves in Fig. A2, the finite element simulation is seen to be in excellent agreement with the analytical solutions (or theoretical results) for this problem.

References

Boyd, D.L., Trainor-Guitton, W., Walton, G., 2018. Assessment of rock unit variability through use of spatial variograms. Eng. Geol. 233, 200–212.
Cai, M., 2011. Rock mass characterization and rock property variability considerations for tunnel and cavern design. Rock Mech. Rock Eng. 44 (4), 379–399.
Çanakci, H., Pala, M., 2007. Tensile strength of basalt from a neural network. Eng. Geol. 94 (1), 10–18.
Chen, S.J., Zhu, W.C., Yu, Q.L., Liu, X.G., 2016. Characterization of anisotropy of joint surface roughness and aperture by variogram approach based on digital image processing technique. Rock Mech. Rock Eng. 49 (3), 855–876.
Eivazy, H., Esmaieli, K., Jean, R., 2017. Modelling Geomechanical Heterogeneity of Rock Masses Using Direct and Indirect Geostatistical Conditional Simulation Methods. Rock Mech. Rock Eng. 50 (12), 3175–3195.
Feng, XiaTing, Chen, BingRui, Yang, C., Zhou, H., Ding, X., 2006. Identification of visco-elastic models for rocks using genetic programming coupled with the modified particle swarm optimization algorithm. Int. J. Rock Mech. Min. Sci. 43 (5), 789–801.
Gao, X., Yan, E.C., Yeh, T.-C.J., Cai, J.-S., Liang, Y., Wang, M., 2018a. A geostatistical inverse approach to characterize the spatial distribution of deformability and shear strength of rock mass around an unlined rock cavern. Eng. Geol. 245, 106–119. https://doi.org/10.1016/j.enggeo.2018.08.007.
Gao, X., Yan, E.-C., Yeh, T.-C.J., Wang, Y.-L., Cai, J.-S., Hao, Y.-H., 2018b. Sequential back analysis of spatial distribution of geomechanical properties around an unlined rock cavern. Comput. Geotechn. 99, 177–190.
Ghorbani, M., Sharifzadeh, M., 2009. Long term stability assessment of Siah Bisheh powerhouse cavern based on displacement back analysis method. Tunnelling Underground Space Technol. 24 (5), 574–583.
Grégoire, Allaire, François, Jouve, Anca-Maria, Toader, 2004. Structural optimization using sensitivity analysis and a level-set method. J. Comput. Phys. 194 (1), 363–393.
Griffiths, D.V., Huang, J., Fenton, G.A., 2009. Influence of Spatial Variability on Slope Reliability Using 2-D Random Fields. J. Geotechn. Geoenviron. Eng. 135 (10), 1367–1378. https://doi.org/10.1061/(ASCE)GT.1943-5606.0000099.
Griffiths, D.V., Huang, J., Fenton, G.a., 2011. Probabilistic infinite slope analysis. Comput. Geotechn. 38 (4), 577–584. https://doi.org/10.1016/j.compgeo.2011.03.006.
Guan, Z., Jiang, Y., Tanabashi, Y., Huang, H., 2008. A new rheological model and its application in mountain tunnelling. Tunnelling Underground Space Technol. Incorporat. Trenchl. Technol. Res. 23 (3), 292–299.
Gutjahr, A.L., 1989. Fast Fourier Transforms for Random Field Generation: Project Report for Los Alamos Grant to New Mexico Tech. New Mexico Institute of Mining and Technology.
Hsu, S.-C., Nelson, P.P., 2006. Material spatial variability and slope stability for weak rock masses. J. Geotechn. Geoenviron. Eng. 132 (2), 183–193.
Illman, W.A., Liu, X., Takeuchi, S., Yeh, T.J., Ando, K., Saegusa, H., 2009. Hydraulic tomography in fractured granite: Mizunami Underground Research site, Japan. Water Resourc. Res. 45 (1).
Jiang, Q., Qi, Y., Wang, Z., Zhou, C., 2013. An extended Nishihara model for the description of three stages of sandstone creep. Geophys. J. Int. 193 (2), 841–854.
Liu, S., Yeh, T.J., Gardiner, R., 2002. Effectiveness of hydraulic tomography: Sandbox experiments. Water Resourc. Res. 38 (4).
Liu, W.F., Leung, Y.F., Lo, M.K., 2016. Integrated framework for characterization of spatial variability of geological profiles. Can. Geotechn. J. 54 (1), 47–58.
Mayer, J.M., Stead, D., 2017. A Comparison of Traditional, Step-Path, and Geostatistical Techniques in the Stability Analysis of a Large Open Pit. Rock Mech. Rock Eng. 50 (4), 927–949.
Nadimi, S., Shahriar, K., Sharifzadeh, M., Moarefvand, P., 2011. Triaxial creep tests and back analysis of time-dependent behavior of Siah Bisheh cavern by 3-Dimensional Distinct Element Method. Tunnelling Underground Space Technol. 26 (1), 155–162.
Nazarova, L.A., Nazarov, L.A., 2005. Estimation of Pillar Stability Based on Viscoelastic Model of Rock Mass. J. Min. Sci. 41 (5), 399–406.
Owen, D. R. J., & Hinton, E. (1980). Finite elements in plasticity: theory and practice.
Paraskevopoulou, C., Diederichs, M., 2018. Analysis of time-dependent deformation in tunnels using the Convergence-Confinement Method. Tunnelling Underground Space Technol. 71, 62–80. https://doi.org/10.1016/j.tust.2017.07.001.
Pellet, F., Roosefid, M., Deleruyelle, F., 2009. On the 3D numerical modelling of the time-dependent development of the damage zone around underground galleries during and after excavation. Tunnelling Underground Space Technol. Incorporat. Trenchl. Technol. Res. 24 (6), 665–674.
Pinheiro, M., Vallejos, J., Miranda, T., Emery, X., 2016. Geostatistical simulation to map the spatial heterogeneity of geomechanical parameters: A case study with rock mass rating. Eng. Geol. 205, 93–103.
Sakurai, S. (1993). Assessment of cut slope stability by means of back analysis of measured displacements. Proc. Int. Sympo. Assessment and Prevention of Failure Phenomena in Rock Engineering, Istanbul, 3–9.
Sakurai, S., 2017. Back Analysis in Rock Engineering. CRC Press.
Sakurai, S. (2000). Back analysis of strain localization occurring in the vicinity of geostructures. Computer Methods and Advances in Geomechanics: Proceedings of the 10th International Conference on Computer Methods and Advances in Geomechanics, Tucson, Arizona, USA, 7-12 January 2001, 67.
Schweiger, H.F., Thurner, R., Pöttler, R., 2001. Reliability analysis in geotechnics with deterministic finite elements—Theoretical concepts and practical application. Int. J. Geomech. 1 (4), 389–413.
Smith, I.M., Griffiths, D.V., Margetts, L., 2013. Programming the finite element method. John Wiley & Sons.
Song, K.I., Cho, G.C., Lee, I.M., Lee, S.W. (2005). The effect of spatial distribution in geotechnical design parameters on tunnel deformation. Underground Space Use. Analysis of the Past and Lessons for the Future, Two Volume Set: Proceedings of the International World Tunnel Congress and the 31st ITA General Assembly, Istanbul, Turkey, 7-12 May 2005, 183.
Song, K.-I., Cho, G.-C., Lee, S.-W., 2011. Effects of spatially variable weathered rock properties on tunnel behavior. Probabilistic Eng. Mech. 26 (3), 413–426.
Sykes, J.F., Wilson, J.L., Andrews, R.W., 1985. Sensitivity Analysis for Steady State Groundwater Flow Using Adjoint Operators. Water Resourc. Res. 21 (3), 359–371.
Xiang, J., Yeh, T.J., Lee, C., Hsu, K., Wen, J., 2009. A simultaneous successive linear estimator and a guide for hydraulic tomography analysis. Water Resourc. Res. 45 (2).
Yang, W.D., Zhang, Q.Y., Zhang, J.G., 2008. Numerical Back Inversion Method of Compressive Creep Parameters of Rock Masses under Rigid Bearing Plate and its Application. Adv. Mater. Res. 33–37, 429–434.
Yang, Z., Wang, Z., Zhang, L., Zhou, R., Xing, N., 2001. Back-analysis of viscoelastic

displacements in a soft rock road tunnel. Int. J. Rock Mech. Min. Sci. 38 (3), 331–341.
Yeh, T.J., Jin, M., Hanna, S., 1996. An iterative stochastic inverse method: Conditional effective transmissivity and hydraulic head fields. Water Resourc. Res. 32 (1), 85–92.
Yeh, T.J., Srivastava, R., Guzman, A., Harter, T., 1993. A Numerical Model for Water Flow and Chemical Transport in Variably Saturated Porous Media. Ground Water 31 (4), 634–644. https://doi.org/10.1111/j.1745-6584.1993.tb00597.x.
Yeh, T.-C.J., Liu, S., 2000. Hydraulic tomography: Development of a new aquifer test method. Water Resourc. Res. 36 (8), 2095–2105. https://doi.org/10.1029/2000WR900114.
Yeh, Tian-Chyi "Jim", Raziuddin, Khaleel, Carroll, Kenneth C., 2015. Flow through Heterogeneous Geologic Media. Cambridge University Press., New York.
Zha, Y., Yeh, T.-C.J., Mao, D., Yang, J., Lu, W., 2014. Usefulness of flux measurements during hydraulic tomographic survey for mapping hydraulic conductivity distribution in a fractured medium. Adv. Water Res. 71, 162–176.
Zhang, Q.Y., Zhang, J.G., Yang, W.D., Ru-Ping, H.E., 2008. Identification of creep model and parameters inversion for soft rock mass. J. Hydraul. Eng. 39 (1), 66–72.
Zhu, J., Yeh, T.-C.J., 2005. Characterization of aquifer heterogeneity using transient hydraulic tomography. Water Resourc. Res. 41 (7).